coatings

MDPI

Article

Effect of Sintering Process on Microstructure and Properties of $(Zr_{0.2}Ta_{0.2}Ti_{0.2}Cr_{0.2}Hf_{0.2})Si_2$ High-Entropy Silicide Ceramics

Zihao Zhang, Huaigan Yi, Mengtian Liang, Linying Xie, Bingbing Yin * and Yi Yang *

School of Materials Science and Engineering, Xiangtan University, Xiangtan 411105, China; 19118002706@163.com (Z.Z.); 18870241990@163.com (H.Y.); liangmengtian7@163.com (M.L.); 17872208913@163.com (L.X.)

* Correspondence: yinbingbing1990@xtu.edu.cn (B.Y.); yangyi@xtu.edu.cn (Y.Y.)

Abstract: In this study, five kinds of $(Zr_{0.2}Ta_{0.2}Ti_{0.2}Cr_{0.2}Hf_{0.2})Si_2$ high-entropy ceramics were prepared by a two-step method under different vacuum pressureless pre-sintering processes, and the microstructures and mechanical properties of the ceramics under different parameters of the pre-sintering process were systematically discussed. The results show that the physical structure of the ceramic samples remains basically unchanged by changing the pre-sintering conditions; the longer the holding time of the initial pre-sintering, the higher the densification of the samples and all of them are above 95%. The hardness of the ceramics was around 10 GPa, with the best hardness of 10.11 GPa at 1300 °C for 3 h. This conclusion provides data support for the optimization of the high-entropy ceramics preparation process.

Keywords: vacuum pressureless sintering; high entropy ceramics; homogeneous density; fracture toughness

check for updates

Citation: Zhang, Z.; Yi, H.; Liang, M.; Xie, L.; Yin, B.; Yang, Y. Effect of Sintering Process on Microstructure and Properties of $(Zr_{0.2}Ta_{0.2}Ti_{0.2}Cr_{0.2}Hf_{0.2})Si_2$ High-Entropy Silicide Ceramics. *Coatings* **2024**, *14*, 1280. https://doi.org/10.3390/coatings14101280

Academic Editor: Günter Motz

Received: 29 August 2024
Revised: 25 September 2024
Accepted: 5 October 2024
Published: 8 October 2024

Copyright: © 2024 by the authors. Licensee MDPI, Basel, Switzerland. This article is an open access article distributed under the terms and conditions of the Creative Commons Attribution (CC BY) license (https://creativecommons.org/licenses/by/4.0/).

1. Introduction

The hot-end components of aerospace devices, as the core building blocks of the whole, must be selected to meet the practical requirements of oxidation resistance, corrosion resistance, and excellent mechanical properties [1,2]. While C/C composites are a class of new engineering materials with ceramic properties but brittle and pseudoplastic characteristics [3,4], by using graphite fibers as reinforcement, and embedding carbon fiber reinforcement in the carbon-based materials, the overall structure not only has the flexible structural designability and good mechanical properties of fiber-reinforced materials, but also has other excellent properties of carbon materials, such as lower coefficient of thermal expansion, high thermal conductivity and electrical conductivity, excellent thermal shock resistance, excellent thermal shock resistance, etc. [5]. It is an indispensable high-temperature material for aerospace and other industrial fields, and is widely used in the fields of throat lining of rocket engines, brake discs of aerospace aircrafts, and thermal protection materials of advanced vehicles [6,7].

However, the main reason limiting the wide application of C/C composites in high temperature fields is that they are oxidized in the oxygenated atmosphere above 450 °C [8,9], which is more prone to damage the overall properties at high temperature, leading to material fracture and failure, affecting the application in the aerospace field. Therefore, oxidation protection of C/C composites is needed. At present, the commonly used means is coating protection on C/C composites, $MoSi_2$ material is currently the largest protective coating for the material to improve the oxidation resistance, $MoSi_2$ material at high temperatures forms a layer of glassy silica, which will flow to protect the material very well. Although $MoSi_2$ has good elasticity and antioxidant properties, the inherent brittleness of $MoSi_2$, as well as its poor creep resistance at 1200 °C–1300 °C, makes it impossible to protect C/C composites for long periods at high temperatures.

In general, there are two important methods to improve oxidation resistance: alloying and surface coating. During the alloying process, protective oxide forming elements such as aluminum, chromium and silicon are often chosen [10–12]. The addition of these elements causes the material to form a dense protective oxide layer on the surface, which prevents oxygen from penetrating inward. In addition to alloying, surface coating is considered to be an effective method to improve antioxidant properties. Among the antioxidant coatings, silicide coatings with high melting points, good thermal stability and self-healing ability are widely used to protect refractory metals. A dense SiO_2 layer is formed on the surface of the coating during oxidation, which hinders the inward diffusion of oxygen [13–15].

Advanced sintering technology is an important means to obtain high-entropy ceramics with good properties. Compared with traditional sintering techniques, the most significant advantage of spark plasma sintering (SPS) [16,17] is the rapid sintering, which often takes only a few minutes or even tens of seconds. However, the sluggish diffusion effect of high-entropy ceramics will have a hindering effect on the diffusion of substances, which may lead to compositional inhomogeneity or non-homogeneous phenomenon of the microstructure of the samples. Therefore, the combination of spark plasma sintering and other sintering techniques has greater advantages, such as the two-step sintering method can effectively inhibit grain coarsening and improve the material properties while obtaining a dense sintered body. Deng et al. [18] successfully prepared single-phase high-entropy $(Y_{0.2}Gd_{0.2}Er_{0.2}Yb_{0.2}Lu_{0.2})_2Zr_2O_7$ materials with excellent mechanical properties by solid-state reaction method and SPS, and the high-entropy ceramics had a hardness of 12.1 ± 0.2 GPa and a fracture toughness of 1.1 ± 0.1 MPa·$m^{1/2}$. The process of pre-sintering can effectively promote the reaction and initial sintering between the ceramic powders to form a dense sintered body, thus providing an optimised microstructural basis for subsequent high-temperature sintering.

In this work, we study the effect of the variation of the pre-sintering process in the two-step sintering method on the microstructure and morphology, phase components and phase distribution of the prepared high-entropy silicide ceramic specimens, and the effect of the preparation process on the relative density, hardness, and fracture toughness of the high-entropy silicide ceramic specimens.

2. Materials and Methods

2.1. Material and Sample Preparation

Zr, Ta, Ti, Cr, Hf and Si powders (99.8% purity, 1 μm, Shanghai Xiangtian Nanomaterials Corporation, Shanghai, China) were used as experimental raw materials, and ball milled in a ball milling tank for 6 h. The mixed powders were first sintered by vacuum pressureless pre-sintering, and then sintered by using SPS on the silicide green body, with the following sintering parameters: holding temperature for 5 min at the sintering node of 900 °C, and holding temperature for 5 min at the final temperature of 1100 °C, and the sintering pressure of 35 MPa, and the samples obtained were respectively named V1, V2, V3, V4, and V5. The specific vacuum pressureless pre-sintering methods are shown in Table 1.

Table 1. Vacuum pressureless pre-sintering process parameters.

Sample Number	Sintering Temperature (°C)	Holding Time (h)
V1	1200	3
V2	1300	3
V3	1400	3
V4	1400	2
V5	1400	4

2.2. Physical and Microstructural Characterization

The samples were characterized by X-ray diffraction ((XRD, Rigaku Ultimate IV, Tokyo, Japan) with Cu Kα radiation at 30 kV to analyze the physical composition of the samples.

The samples were characterized by scanning electron microscope (SEM, EVO MA10, ZEISS, Jena, Germany) equipped with energy-dispersive X-ray spectroscopy (EDS, X-Max, Oxford, UK) to analyze the microstructure and morphology of the samples.

Density tests were carried out using the Archimedes drainage method to calculate the bulk density of the ceramic materials. Relative density is the ratio of the actual density of the sample to the theoretical density. The theoretical density was calculated as 6.42 g/cm^3 by the rule of mixtures [19].

2.3. Mechanical Characterization (Hardness & Fracture Toughness Experiments)

A Vickers hardness tester (SHYCHVT-30Z, Laizhou Huayin Testing Instrument Company, Laizhou, China) was used to test the samples. The Vickers hardness of the samples was tested under a load of 50 N. The time of testing was kept at approximately 15 s. Each test specimen was tested with 5–10 data points at different positions to ensure that the error of the data was negligible and the results were averaged. The results were averaged. According to the diamond-shaped indentation and cracks produced by the indenter on the surface of the sample after applying the load, the sample was calculated. The fracture toughness of the sample is calculated according to the diamond-shaped indentation and cracks produced on the sample surface after the indenter is pressed into the sample after the load is applied. Vickers hardness and fracture toughness of the sample are calculated using the following Formula (1).

In the scanning electron microscope to observe the rhombic indentation of the two diagonal lengths, and recorded as a1 and a2, from the rhombus in the direction of the various diagonals to extend that is the indentation crack, recorded as c1 and c2, as shown in Figure 1; according to the relevant experimental data, brought into the Equation (1) to find the specimen's fracture toughness [20]:

$$K_{IC} = 0.203 \times \sqrt{\frac{a_1 + a_2}{2}} \times \left(\frac{c_1 + c_2}{a_1 + a_2}\right)^{-3/2} \times HV \quad (1)$$

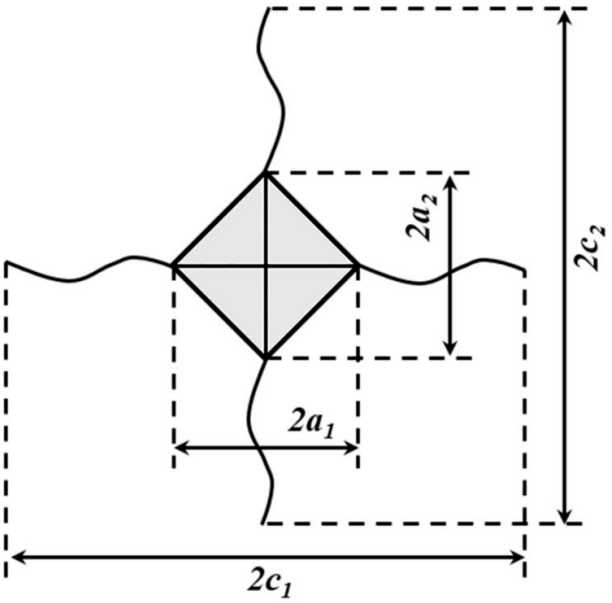

Figure 1. Schematic diagram of indentation and cracking for Vickers hardness.

3. Experimental Results and Analysis

3.1. Effect of Pressureless Pre-Sintering Temperature on the Physical Phase and Microstructure of High-Entropy Silicide Ceramics

Figure 2 shows the XRD diagrams of V1, V2, and V3 high-entropy silicide ceramics. When the pressureless pre-sintering temperature was 1200 °C, the ceramic specimens

formed (Hf, Zr) Si_2 solid solution, (Ta, Ti, Cr)Si_2 solid solution and (Hf, Zr) solid solution. With the gradual increase in temperature, the unreacted elemental Si diffraction peaks and (Hf, Zr) solid solution diffraction peaks in the gradual weakening, when the temperature reaches 1400 °C, the diffraction peaks of the V3 ceramic specimen relative to the other two ceramic specimens become more, which also formed a certain proportion of high entropy phase, and the diffraction peaks of ZrSi were observed, ZrSi is not fully integrated into the (Hf, Zr)Si_2 solid solution. The diffraction peaks of the V2 ceramic specimen are the smoothest, and compared to the V1 ceramic specimen, the elements in the V2 ceramic specimen were diffused more sufficiently, which exacerbates the integration of the solid solution. The diffraction in the V3 appeared with more peaks, which made the two main solid solution phases in the high-entropy silicide ceramics more distinct and more obvious with the further increase in temperature. From the three diffraction lines, it can be seen that the diffraction peaks of (Hf, Zr)Si_2 solid solution and (Ta, Ti, Cr)Si_2 solid solution occupy the vast majority of the diffraction peaks, and the diffraction peaks are also the strongest.

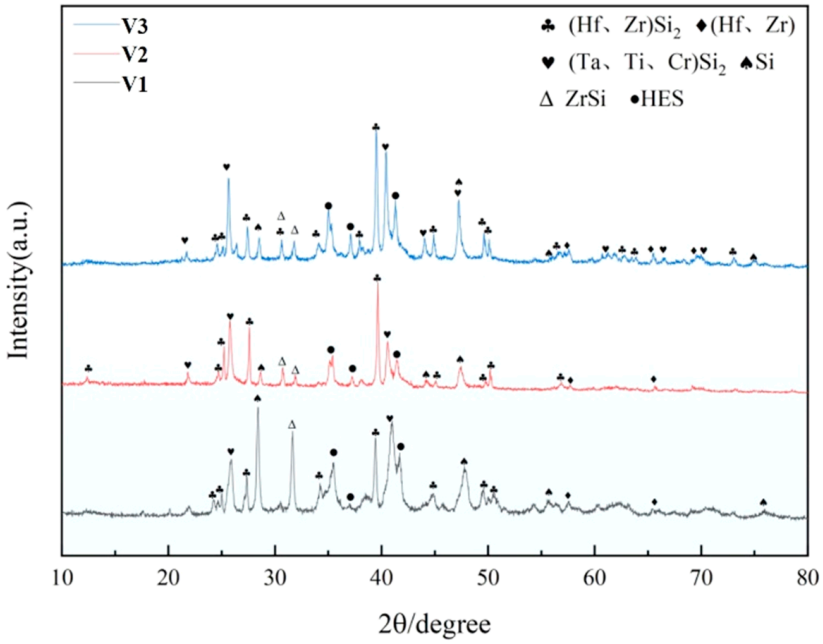

Figure 2. XRD patterns of V1, V2, and V3 high-entropy silicide ceramics.

Figure 3 shows the microscopic morphologies of the V1 ceramic specimen. From Figure 3a, it can be seen that the overall V1 ceramic specimen is not homogeneous enough, the specimen has a lot of large black holes, and the elemental distribution of the sample is not completely homogeneous; From the EDS mappings of Figure 3b, the elements such as Ta, Ti, and Cr are basically enriched, and the elements such as Zr, and Hf are enriched, and most of the Si elements are enriched in the elements such as Ta, Ti, and Cr, and a small portion elements such as Zr, Hf, etc., which coincides with the XRD diagrams of high-entropy silicide ceramics; this enrichment can be more clearly found by SEM and EDS in Figure 3c. It can also be observed from Figure 3c of the V1 specimen that the specimen shows an overall light gray uniformly enriched Hf, Zr and Si phases and dark gray Ta, Ti, Cr and Si particles; in addition to these two overall phases, the V1 ceramic specimen also has a diffusely distributed white granular phase.

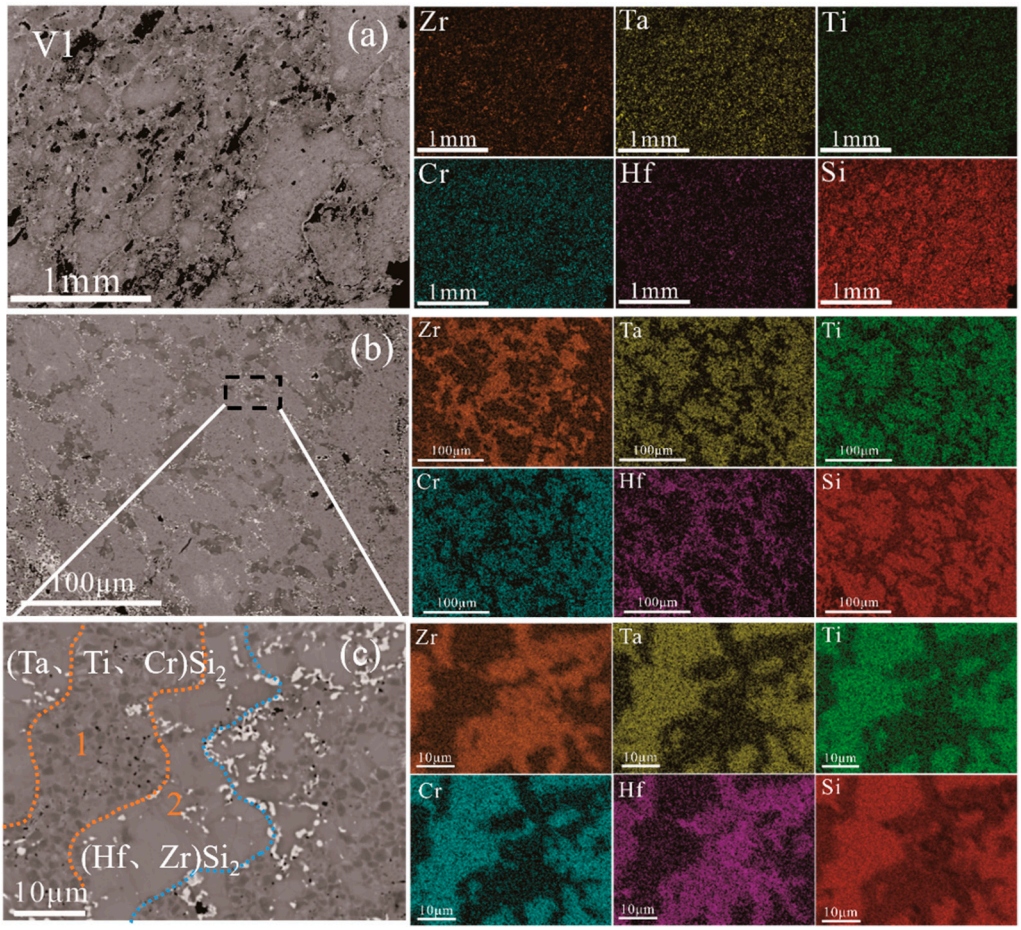

Figure 3. Micro-morphologies of V1 high-entropy silicide ceramics: (**a**) 100×; (**b**) 1000×; (**c**) 5000×.

The EDS point-scanning energy spectroscopy results of the light-gray Hf, Zr, and Si elementally homogeneous enriched phases and the dark-gray particles of the Ta, Ti, Cr, and Si elementally enriched phases are shown in Table 2, where it is inferred that the light-gray homogeneous phases are the solid solutions of $ZrSi_2$ and $HfSi_2$ based on the atomic fraction ratios of the individual elements of the point 2 [21], and that the dark-gray particles Ta, Ti, Cr, and Si element-enriched phases are solid solutions formed by $TaSi_2$, $TiSi_2$, and $CrSi_2$ as well as the unreacted element Si. This speculation is supported by the (Ta, Ti, Cr)Si_2 solid solution [22] and the Si element on one diffraction peak shown in the XRD of Figure 2.

Table 2. EDS energy spectrum results of the 2 positions labeled in Figure 3c.

Labeling Area/Element Atomic Fraction (at. %)	Zr	Ta	Ti	Cr	Hf	Si
1	1.3	9.1	7.7	7.0	1.8	73.1
2	19.2	0.1	2.3	0.3	11.7	66.4

Figure 4 shows the microscopic morphologies of the V2 ceramic specimen. As can be seen from the SEM and EDS of Figure 4a, the sample is very homogeneously fused, and the six elements are uniformly distributed on the surface of the specimen without any obvious aggregation, and the pores of the sample are very small compared to the V1 ceramic specimen. In the V2 ceramic specimen, the light gray and dark gray solid solutions are interspersed with each other to form a whole, and no obvious white particles can be seen under low magnification. According to the SEM and EDS results in Figure 4b, the white particles gradually appear, but they are still very fine and diffusely distributed on

the sample surface, and the silver-gray color, which is intermediate between the light-gray and dark-gray colors, also appears in both main phases, and the silver-gray color is observed in the EDS. In the EDS mappings of Figure 4b, the six elements in the silver-gray phase sparsely appear as small dots, and it is presumed that the silver-gray phase is a high-entropy phase. The white granular phase appears to be enriched in two elements, Hf and Zr, and it is presumed that the white granular phase is a (Hf, Zr) solid solution phase [23]. The energy spectrum points scan of point 3, 4, and 5 of Figure 4c are shown in Table 3, and the energy spectrum results of point 3 confirm that the white particles are (Hf, Zr) solid solution phase. Point 4 and 5 correspond to the presumed silver-gray phase.

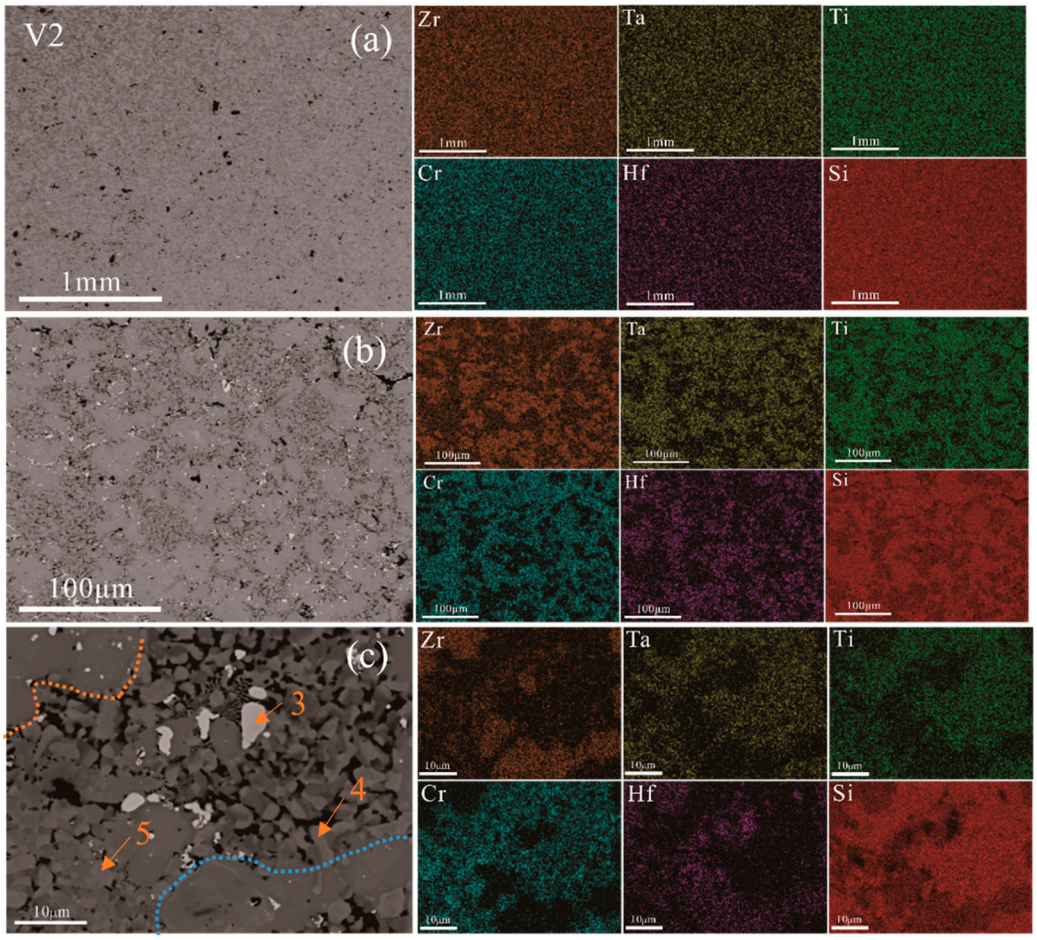

Figure 4. Micro-morphologies of V2 high-entropy silicide ceramics: (**a**) 100×; (**b**) 1000×; (**c**) 5000×.

Table 3. EDS energy spectrum results of the 3 positions labeled in Figure 4c.

Labeling Area/Element Atomic Fraction (at. %)	Zr	Ta	Ti	Cr	Hf	Si
3	6.5	-	-	0.8	92.7	-
4	2.8	10.7	8.2	5.8	3.5	69.0
5	3.2	10.1	7.2	8.1	4.6	66.8

Figure 5 shows the microscopic morphologies of the V3 ceramic specimen. As shown in Figure 5a, the overall structure of the V3 ceramic specimen becomes rougher, and there are no obvious large pores compared to V2, but the overall number of pores has increased a lot. The two main phases of the V3 ceramic specimen are uniformly distributed shown in Figure 5b, and the light-gray (Hf, Zr) Si_2 solid solution phase and dark gray particles of (Ta, Ti, Cr)Si_2 solid solution phase are hierarchically and uniformly distributed on the

sample surface. Compared with V2, the dark gray particles of (Ta, Ti, Cr)Si_2 solid solution phase are obviously increased, and the overall size of the particles is larger and darker in color. V2 ceramic specimens in Figure 4b appear to be almost all uniformly light gray (Hf, Zr) Si_2 solid solution phase is diffusely distributed, while the V3 ceramic specimen in Figure 5b looks obviously granular phase occupies the surface of the sample. Figure 5c shows that the V3 ceramic specimen has some large white particles, and there are also some finer white particles among the large white particles, and the large white particles are not completely and uniformly fused together, and the particles have a lot of dark-coloured irregularly rounded distributions, as well as some holes.

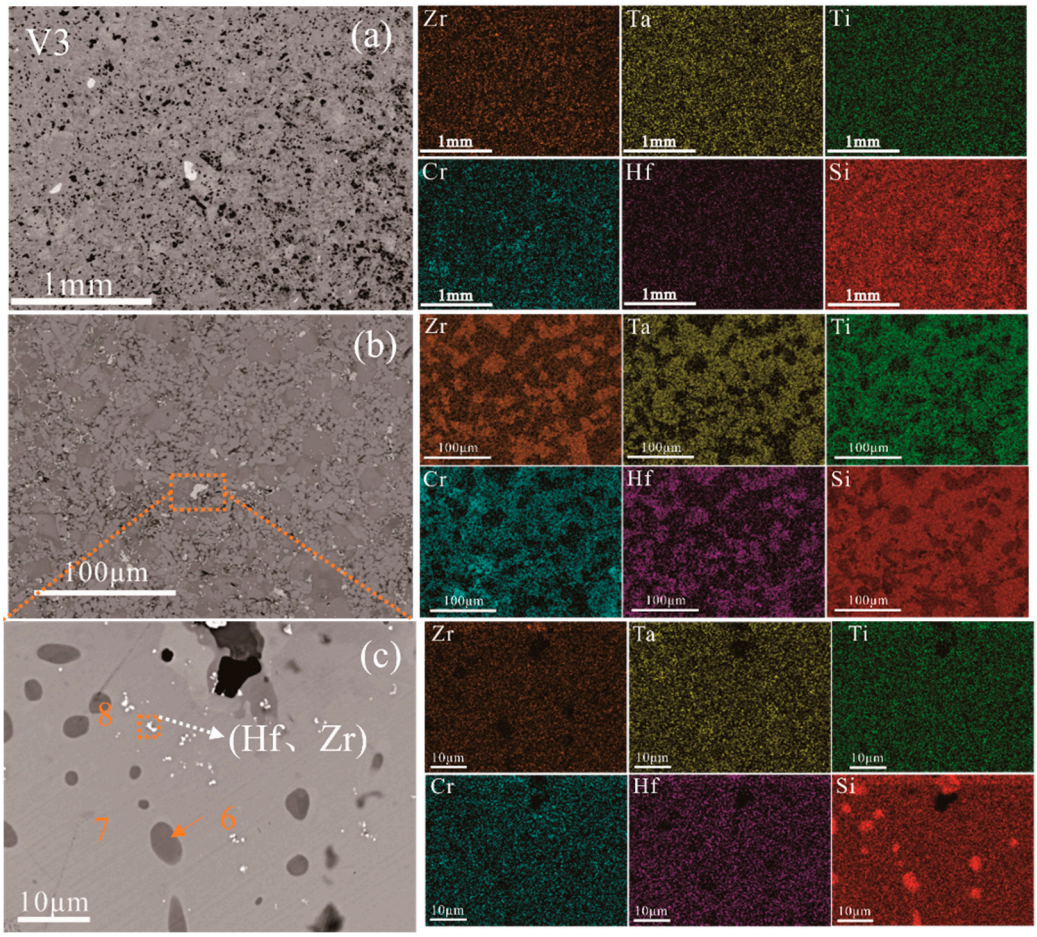

Figure 5. Micro-morphologies of V3 high-entropy silicide ceramics: (**a**) 100×; (**b**) 1000×; (**c**) 5000×.

The EDS point-scan spectras of the large white particle phase and the small white particle phase are shown in Table 4. The small white particle phase is presumed to be a (Hf, Zr) solid solution phase based on the atomic fraction ratios of each element of the point 8, which is consistent with the point 3 in Table 3. According to the EDS results of Figure 5c, it can be found that Ta and Si elements are enriched in the dark irregular circles, and point 6 is its point scan result, which speculates that the dark gray irregular circle is the high entropy phase, while according to the energy spectrum result of point 7, the atomic proportion of metal elements occupies about 50%, and the atomic proportion of Si elements occupies about 50%, which speculates that the large white particles are monosilicides [24].

Table 4. EDS energy spectrum results of the 3 positions labeled in Figure 5c.

Labeling Area/Element Atomic Fraction (at. %)	Zr	Ta	Ti	Cr	Hf	Si
6	2.2	14.2	7.8	2.8	4.3	68.7
7	10.8	10.4	11.5	6.7	13.2	47.4
8	10.9	-	-	2.3	86.8	-

3.2. Effect of Holding Time of Pressureless Pre-Sintering on the Physical Phase and Microstructure of High Entropy Silicide Ceramics

Figure 6 shows the XRD patterns of V3, V4 and V5 high entropy silicide ceramics. From the Figure 6, the physical phases formed in the ceramic specimens under the holding time of 2 h are (Hf, Zr)Si_2 solid solution, (Ta, Ti, Cr)Si_2 solid solution, and a small amount of high entropy phase. As the holding time increases, the diffraction peaks of (Hf, Zr) solid solution, ZrSi, and incompletely reacted elements of Si appear in the XRD diagram, and the intensity of the diffraction peaks of several phases is relatively weak. It can also be observed in the figure that the diffraction peaks of the V4 ceramic specimen with a holding time of 2 h are very few, which is because the holding time of 2 h is too short during the initial sintering, the green body is not sufficiently sintered, and the bonding between the particles is not strong enough, and the formation of the green body is not sufficiently strong because of the short sintering time. The diffraction peak intensity of (Ta, Ti, Cr)Si_2 solid solution of V5 ceramic specimen with holding time of 4 h gradually becomes weaker compared with that of V3, and the diffraction peak intensity of (Hf, Zr)Si_2 solid solution gradually becomes stronger, which can be seen from the SEM image of V3 ceramic specimen in Section 3.1. The diffraction peaks of the ceramic specimens became more and more numerous as the holding time was extended.

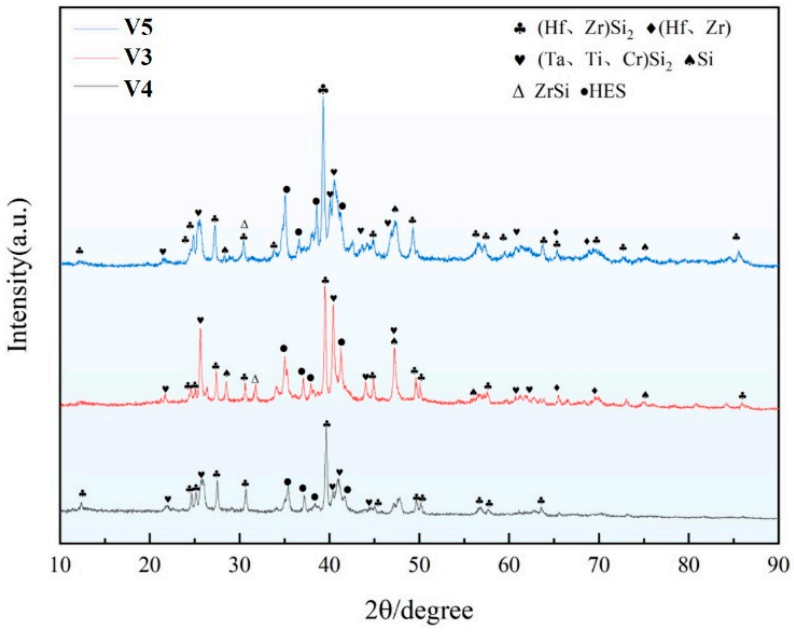

Figure 6. XRD patterns of V3, V4 and V5 high entropy silicide ceramics.

Figure 7 shows the microstructures of the V4 ceramic specimen. As shown in Figure 7a, the sample has many black holes, and the white particles are almost invisible at low magnification, and the overall color is not uniformly distributed. In Figure 7b, it can be seen even more that the overall bonding of the V4 ceramic sample is not homogeneous, and the (Hf, Zr)Si_2 solid solution and (Ta, Ti, Cr)Si_2 solid solution are all randomly scattered on the surface of the sample, and the sample possesses a lot of grayish-white particles. However, it is not obvious to be observed in Figure 7a, which means that the grayish-white

particles are of very small sizes, and the above mentioned in Section 3.1 also explains that the grayish-white color is a part of the high entropy phase. The elemental distribution of the V4 ceramic samples is relatively inhomogeneous, as shown in Figure 7c, the individual elements are diffusely distributed and disordered, and this phenomenon is related to the retention time of V4. The holding time is too short, and the phases formed in the raw billet do not have time to fuse, and the bonding under SPS sintering is weak, resulting in a non-uniform distribution of the phases.

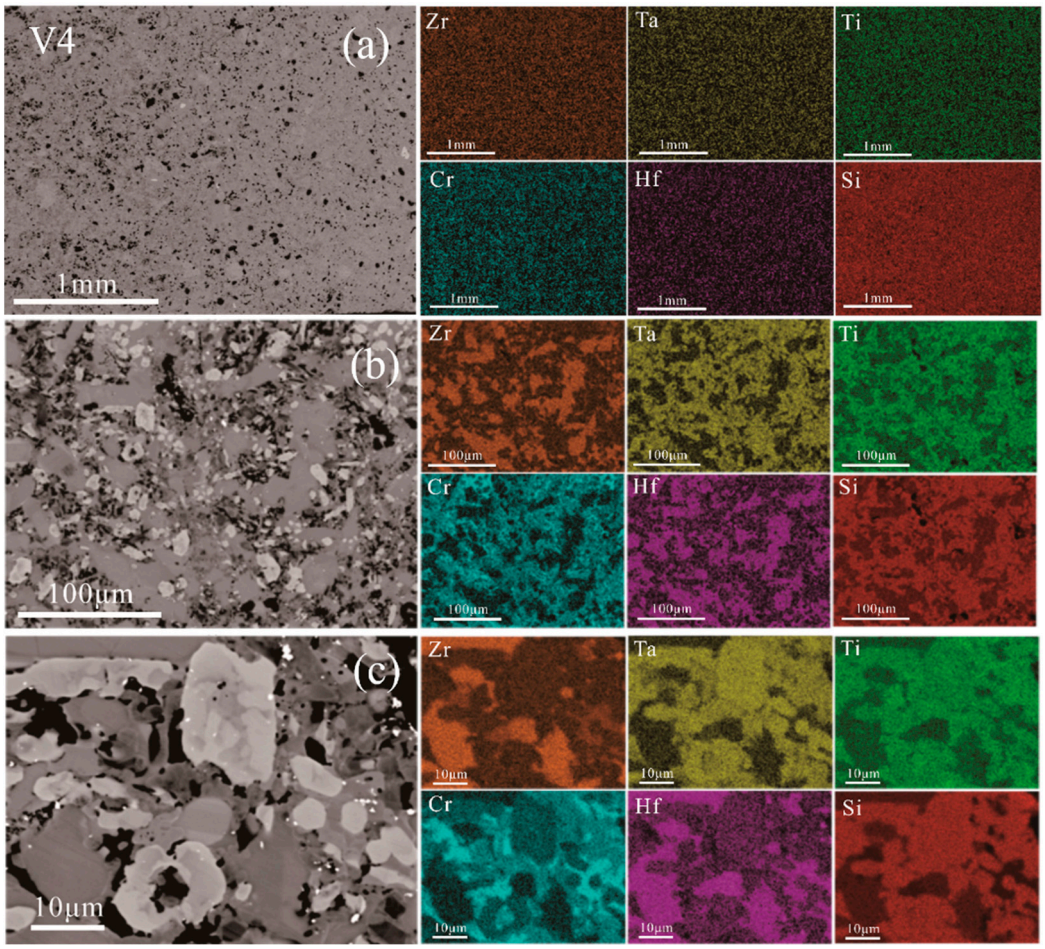

Figure 7. Micro-morphologies of V4 high-entropy silicide ceramics: (**a**) 100×; (**b**) 1000×; (**c**) 5000×.

Figure 8 shows the microscopic morphologies of the V5 ceramic specimen, as shown in Figure 8a, there are many large white particles on the surface of the V5 specimen. The sizes of the particles can be clearly observed in Figure 8a, which indicates that the large white particles are very aggregated, and the number of high-entropy phase particles of the V5 ceramic specimen has a significant increase compared to that of the V4 ceramic. The longer the holding time of the pressureless pre-sintering, the more high entropy phase particles are induced to form, so that the aggregation phenomenon is caused by high entropy phase particles. As can be seen from Figure 8b, the high-entropy phase particles of the ceramic specimens increase, in addition, the light gray uniform phase is more widely distributed compared to Figure 5b, which confirms that the diffraction peak intensity of (Hf, Zr)Si_2 solid solution becomes stronger with the increase of holding time in Figure 6. The corresponding EDS results of the markers in Figure 8c are shown in Table 5. From Figure 8c, it can be seen that the sample is almost a light gray homogeneous phase except for the large white granular phase, and according to the EDS results of point 11, the light gray homogeneous phase is basically the (Hf, Zr)Si_2 solid solution, and with the increase of

the holding time, the (Hf, Zr)Si_2 solid solution is gradually fused and homogeneous. The (Hf, Zr)Si_2 solid solution described in points 9 and 10 is the silver-gray high-entropy phase.

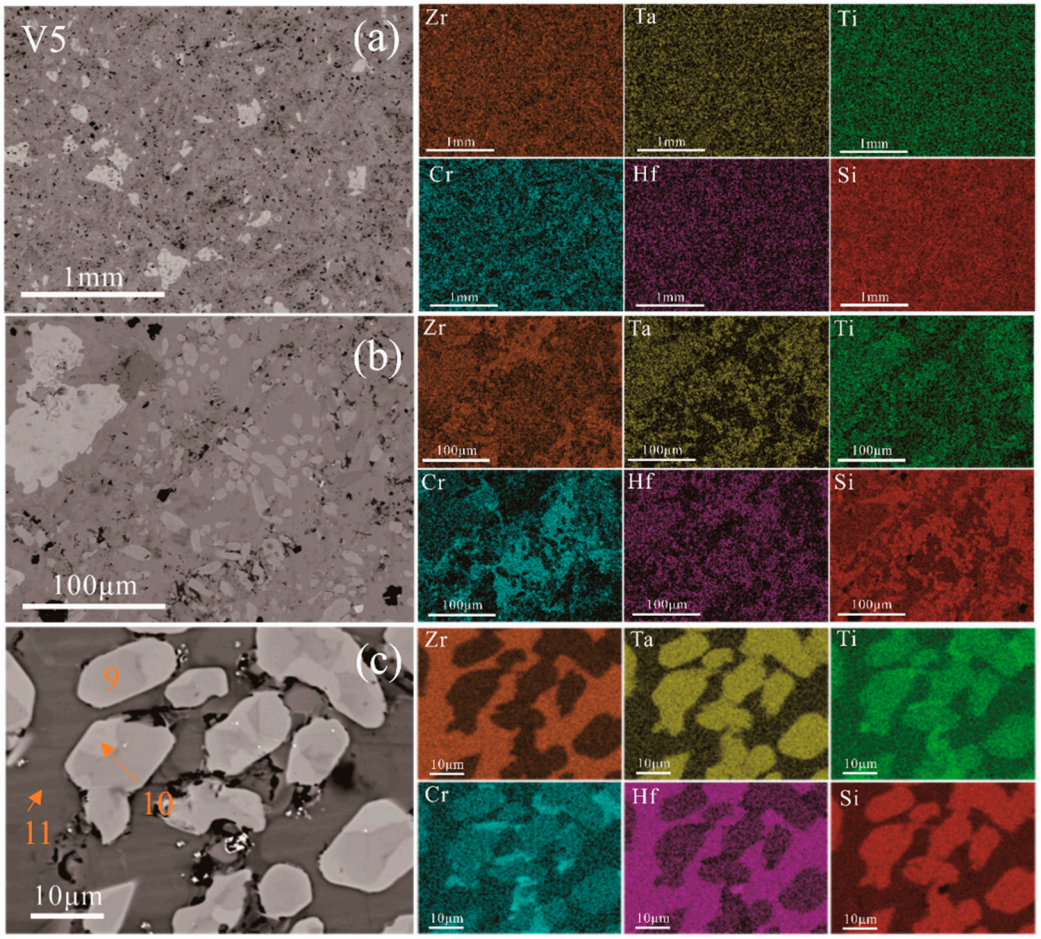

Figure 8. Micro-morphologies of V5 high-entropy silicide ceramics: (**a**) 100×; (**b**) 1000×; (**c**) 5000×.

Table 5. EDS energy spectrum results of the 3 positions labeled in Figure 8c.

Labeling Area/Element Atomic Fraction (at. %)	Zr	Ta	Ti	Cr	Hf	Si
9	3.2	14.5	7.0	1.8	4.3	69.2
10	3.3	15.8	6.4	1.6	4.0	68.9
11	19.3	0.2	3.0	-	13.0	64.5

From the SEM and EDS images of V3, V4, and V5 ceramic specimens, the increase of the holding time of the two-step sintering in the pressureless pre-sintering helps the fusion of the phases in the silicide ceramics, and the holding time of the ceramics will be basically homogeneous fusion of the phases in the ceramics in 3 h or more. The longer the holding time, the more the (Hf, Zr)Si_2 solid solution phases and high-entropy phases will be formed, and conversely, the less (Ta, Ti, Cr)Si_2 solid solution phases are formed.

3.3. Densities and Mechanical Properties of High-Entropy Silicide Ceramics

3.3.1. Effect of Two-Step Sintering Process on Densification

The densities of ($Zr_{0.2}Ta_{0.2}Ti_{0.2}Cr_{0.2}Hf_{0.2}$)$Si_2$ high-entropy silicide ceramics were tested by the Archimedes drainage method, and then the theoretical densities of each disilicide component of ceramic specimens were calculated to obtain the theoretical density values.

Based on the density values of each disilicide component in the ceramic specimen, the theoretical density values of the entire high-entropy silicide ceramic specimen were calculated. The ratio of the actual density to the theoretical density of the high-entropy silicide ceramic specimen is the density of the high-entropy silicide ceramic. Figure 9 shows the densities of high entropy silicide ceramics under different pressureless pre-sintering processes.

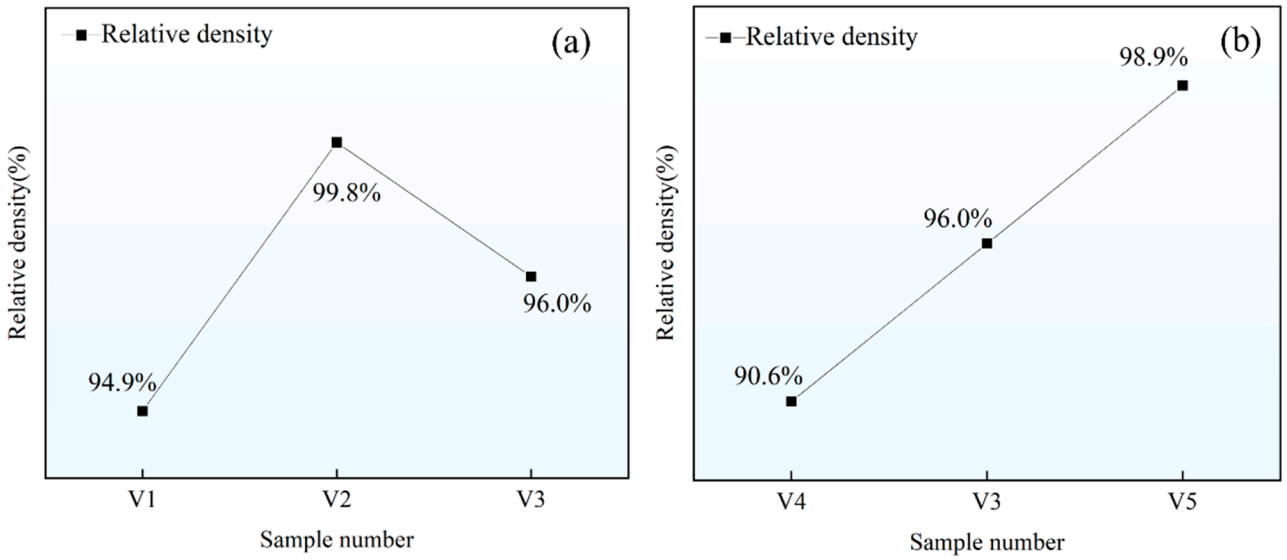

Figure 9. Relative densities of high entropy silicide ceramics under different vacuum pressureless sintering processes: (**a**) densities of ceramic specimens of V1, V2, and V3; (**b**) densities of V3, V4, and V5.

From Figure 9a, the densities of ceramic specimens V1, V2, and V3 are 94.9%, 99.8%, and 96.0% when the temperature of the pressureless pre-sintering is 1200 °C, 1300 °C, and 1400 °C. The trend of the increase of the densities shows a triangular shape, which is firstly increasing and then decreasing. However, if the temperature is too high, the density of the ceramic samples will be reduced, especially if the temperature is 1400 °C, the density of sample V3 will be reduced to 96.0%; the densification results of V1 indicate that if the temperature is too low, the green body of the unpressurised pre-sintered green body in the two-stage sintering of the SPS will be insufficiently sintered, which will affect the subsequent effect of the SPS. At low temperatures, the sintering could not achieve sufficient particle bonding and combination, resulting in the formation of green bodies with insufficient strength to maintain their integrity during the SPS process, which ultimately led to the formation of silicide ceramic specimens with low densification after SPS. And the densification results of V3 indicate that too high a temperature may cause excessive particle growth and the sintering between particles may not be uniform, thus affecting the densification of ceramic specimens.

From Figure 9b, when held for 2 h and 4 h at a vacuum pressureless sintering temperature of 1400 °C, the densities of the ceramic specimens of V3, V4 and V5 were 90.6%, 96.0% and 98.9%, respectively. From the values of the densities of V3, V4 and V5, the best is achieved by holding the heat for 4 h at a vacuum pressureless sintering temperature of 1400 °C, the second is the heat for 3 h, and the worst is the heat for 2 h. The reason for the worst heat for 2 h is that the green body does not have enough time to complete the appropriate pre-sintering, resulting in an insufficiently strong bond between the particles, which affects the formation of the silicide ceramic specimens after SPS. The trend of the curves and the numerical comparisons in Figure 8 shows that both the sintering temperature and the holding time of the pre-sintering in the two-stage sintering of SPS have a great influence on the densification of the ceramic specimens.

3.3.2. Effect of Two-Step Sintering Process on Hardness and Fracture Toughness

Figure 10 shows the relationship between hardness and fracture toughness of high entropy silicide ceramics under different pressureless pre-sintering processes. The hardness of V1, V2 and V3 ceramic specimens was 10.06 GPa, 10.11 GPa and 9.83 GPa, respectively, and the corresponding fracture toughness was 3.27 MPa·m$^{1/2}$, 2.69 MPa·m$^{1/2}$ and 4.04 MPa·m$^{1/2}$, respectively. The trend of the curves in the Figure 10 shows that the hardness of ceramic specimens increases and then decreases with increasing temperature, and the fracture toughness curves show the opposite trend. As the sintering temperature increases, internal pores close, enhancing grain bonding and reducing grain boundaries, which boosts material density and hardness while decreasing fracture toughness [25–27]. However, excessively high temperatures lead to excessive grain growth and a reduction in grain boundary area, which leads to a decrease in hardness and an increase in fracture toughness as grain boundaries are effective barriers to dislocation movement [28,29]. As shown in Figure 10b, when pressureless pre-sintering was carried out at 1400 °C, the hardness of V4 and V5 ceramic specimens held for 2 h and 4 h was 9.46 GPa and 9.04 GPa, respectively, and the corresponding fracture toughness was 4.19 MPa·m$^{1/2}$ and 4.53 MPa·m$^{1/2}$, respectively. The hardness curve in Figure 10b shows the trend of increasing and then decreasing, while the fracture toughness shows the opposite law. Extending the holding time promotes grain diffusion and rearrangement, enhancing densification and hardness [30,31]. However, grain growth reduces the grain boundary area, which can decrease fracture toughness. If the holding time increases beyond a critical point, grain size may further reduce hardness. Nevertheless, longer holding times can also strengthen grain boundaries, preventing crack propagation and improving fracture toughness [32]. V2 ceramic samples of the highest hardness value when the holding temperature is 1300 °C.

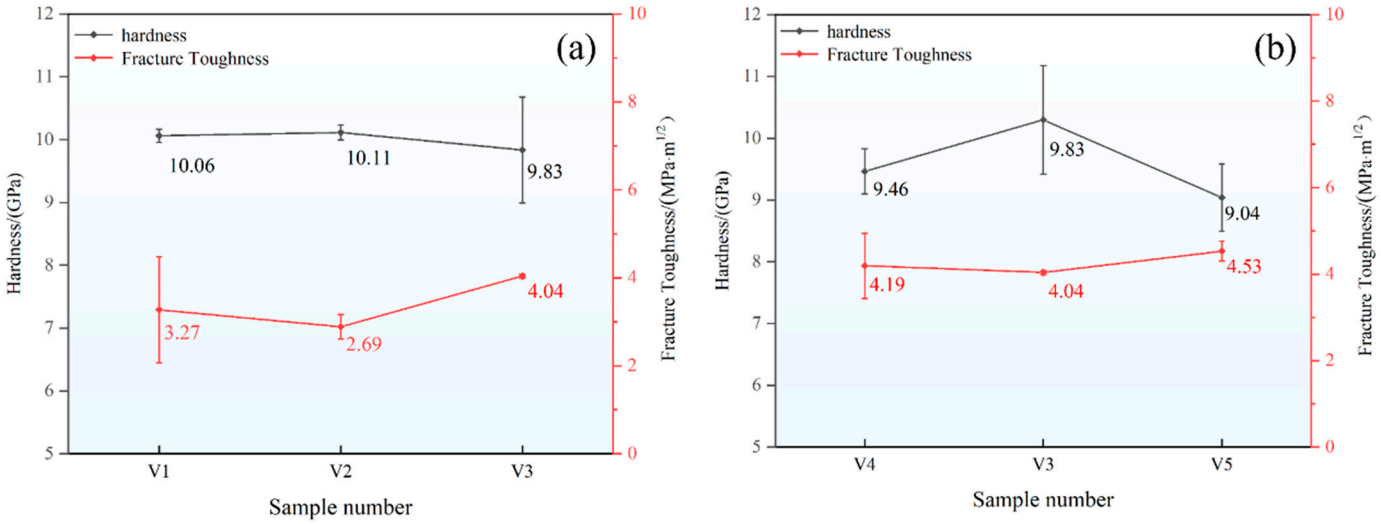

Figure 10. Relationships between the hardness and fracture toughness of high entropy silicide ceramics under different vacuum pressureless sintering processes: (**a**) V1, V2 and V3; (**b**) V3, V4 and V5.

Figure 10 shows that the overall hardness of the ceramic specimens is approximately below 10 GPa, and the fracture toughness varies between 2.69 and 4.53 MPa·m$^{1/2}$. Table 6 shows the comparison of hardness and fracture toughness of disilicides and high entropy disilicides. The hardness of $(Zr_{0.2}Ta_{0.2}Ti_{0.2}Cr_{0.2}Hf_{0.2})Si_2$ shows a significant increase in hardness compared to $MoSi_2$. Compared with other high-entropy disilicides, the hardness of $(Zr_{0.2}Ta_{0.2}Ti_{0.2}Cr_{0.2}Hf_{0.2})Si_2$ maintains a small difference from that of other high-entropy disilicides while the fracture toughness is also significantly improved. This indicates that the two-step method using pressureless pre-sintering combined with SPS can achieve a balance between hardness and fracture toughness, and keep both of them at a favourable

level. Due to the Vickers hardness tester in the collection of data when the collection point of the rhombus is irregular, and there is a small error in the length of the rhombus at the time of collection, so that the hardness and fracture toughness of the error bar is larger. Comparison of the two figures (i.e., Figure 10a,b) shows that the high-entropy silicide ceramics prepared by the two-step sintering method have good mechanical properties, and changing the pressure-free preheating temperature and holding time of the two-step sintering has little effect on the overall mechanical properties of the ceramic specimens.

Table 6. Hardness and fracture toughness of silicide ceramics.

Ceramics		HV(GPa)	K_{IC}(MPa·m$^{1/2}$)
$(Zr_{0.2}Ta_{0.2}Ti_{0.2}Cr_{0.2}Hf_{0.2})Si_2$ (this work)	V1	10.06	3.27
	V2	10.11	2.69
	V3	9.83	4.04
	V4	9.46	4.19
	V5	9.04	4.53
$MoSi_2$-based [33]	$MoSi_2$	8.82	-
	(Mo, 2.5%Re)Si_2	10.19	-
	(Mo, 1%Re) (Si, 2%Al)$_2$	7.14	-
	Mo(Si, 2%Al)$_2$	7.15	-
	(Mo, 1%Nb)Si_2	7.14	-
$(Mo_{0.2}W_{0.2}Cr_{0.2}Ta_{0.2}Nb_{0.2})Si_2$ [34]		11.28	2.55
$(NbMoTa_0W)Si_2$ [35]		11.3	2.68
$Mo_{0.2}Cr_{0.2}Ta_{0.2}Nb_{0.2}W_{0.2}Si_2$ [36]		11.28	2.55
Rule-of-mixture average of five metal disilicides [37]		9.32	-

4. Conclusions

In this paper, the high-entropy silicide ceramics prepared under different vacuum pressureless pre-sintering parameters were microscopically characterised and tested for mechanical properties, and the following conclusions were drawn:

(1) There was no change in the physical phase structure of the silicide ceramic samples prepared by two-step sintering, and the longer the holding time of pressureless pre-sintering the higher the densification of the samples, and in the variable of varying the holding time, the samples with the preliminary sintering at 1400 °C and the holding time of 4 h were the most effective in the preparation of the samples;

(2) The densities of the silicide ceramics prepared by two-step sintering above 90%; the hardnesses of the ceramic specimens of two-step sintering V1, V2, and V3 were 10.06, 10.11, and 9.83 GPa, respectively, and the corresponding fracture toughnesses were 3.27, 2.69, and 4.04 MPa·m$^{1/2}$. The hardness of the V4 and V5 ceramic specimens was 9.46 and 9.04 GPa, respectively, and the corresponding fracture toughness was 4.19 and 4.53 MPa·m$^{1/2}$.

Author Contributions: Conceptualization, Z.Z., H.Y., B.Y. and Y.Y.; Methodology, H.Y. and M.L.; Validation, B.Y.; Formal analysis, Z.Z. and L.X.; Investigation, H.Y. and L.X.; Data curation, M.L.; Writing—original draft, Z.Z.; Writing—review & editing, M.L. and Y.Y.; Supervision, B.Y.; Project administration, B.Y. and Y.Y. All authors have read and agreed to the published version of the manuscript.

Funding: This work was supported by Science and Technology on Advanced Ceramic Fibers and Composites Laboratory, National University of Defense Technology (WDZC20225250503).

Institutional Review Board Statement: Not applicable.

Informed Consent Statement: Not applicable.

Data Availability Statement: Data will be made available on request.

Conflicts of Interest: The authors declare that they have no known competing financial interests or personal relationships that could have appeared to influence the work reported in this paper.

References

1. Kasim, K.; Muley, A.; Stoia, M.; Ladeinde, F. Advanced heat transfer devices for aerospace applications. In Proceedings of the ASME International Mechanical Engineering Congress and Exposition, Tampa, FL, USA, 3–9 November 2017; American Society of Mechanical Engineers: New York, NY, USA, 2017.
2. Patterson, R.L.; Hammoud, A.; Elbuluk, M. Electronic components for use in extreme temperature aerospace applications. In Proceedings of the 12th International Components for Military and Space Electronics Conference (CMSE 08), San Diego, CA, USA, 11–14 February 2008.
3. Virgil'ev, Y.S.; Kalyagina, I. Carbon–carbon composite materials. *Inorg. Mater.* **2004**, *40* (Suppl. 1), S33–S49. [CrossRef]
4. Labruquère, S.; Bourrat, X.; Pailler, R.; Naslain, R. Structure and oxidation of C/C composites: Role of the interface. *Carbon* **2001**, *39*, 971–984. [CrossRef]
5. Zhu, X.; Zhang, Y.; Zhang, J.; Li, T.; Jung, I.-H.; Su, Y.; Gai, W. A low-temperature prepared composite coating to protect SiC-coated C/C composites against oxidation in a wide temperature range for long-life service. *J. Eur. Ceram. Soc.* **2023**, *43*, 4349–4362. [CrossRef]
6. Wang, P.; Zhang, M.; Sun, W.; Ren, X. Oxidation protection of B4C modified HfB_2-SiC coating for C/C composites at 1073–1473 K. *Ceram. Int.* **2022**, *48*, 3206–3215. [CrossRef]
7. Zhou, W.; Xiao, P.; Luo, W.; Li, Y. Microstructural evolution of SiC coating on C/C composites exposed to 1500 °C in ambient air. *Ceram. Int.* **2019**, *45*, 854–860. [CrossRef]
8. McKee, D. Oxidation behavior and protection of carbon/carbon composites. *Carbon* **1987**, *25*, 551–557. [CrossRef]
9. Jin, X.; Fan, X.; Lu, C.; Wang, T. Advances in oxidation and ablation resistance of high and ultra-high temperature ceramics modified or coated carbon/carbon composites. *J. Eur. Ceram. Soc.* **2018**, *38*, 1–28. [CrossRef]
10. Senkov, O.; Woodward, C.; Miracle, D. Microstructure and properties of aluminum-containing refractory high-entropy alloys. *Jom* **2014**, *66*, 2030–2042. [CrossRef]
11. Senkov, O.N.; Senkova, S.V.; Woodward, C.; Miracle, D.B. Low-density, refractory multi-principal element alloys of the Cr-Nb-Ti-V-Zr system: Microstructure and phase analysis. *Acta Mater.* **2013**, *61*, 1545–1557. [CrossRef]
12. Senkov, O.; Senkova, S.; Miracle, D.; Woodward, C. Mechanical properties of low-density, refractory multi-principal element alloys of the Cr-Nb-Ti-V-Zr system. *Mater. Sci. Eng. A* **2013**, *565*, 51–62. [CrossRef]
13. Sun, J.; Fu, Q.G.; Guo, L.P.; Wang, L. Silicide coating fabricated by HAPC/SAPS combination to protect niobium alloy from oxidation. *ACS Appl. Mater. Interfaces* **2016**, *8*, 15838–15847. [CrossRef] [PubMed]
14. Knittel, S.; Mathieu, S.; Portebois, L.; Drawin, S.; Vilasi, M. Development of silicide coatings to ensure the protection of Nb and silicide composites against high temperature oxidation. *Surf. Coat. Technol.* **2013**, *235*, 401–406. [CrossRef]
15. Sakidja, R.; Park, J.; Hamann, J.; Perepezko, J.H. Synthesis of oxidation resistant silicide coatings on Mo-Si-B alloys. *Scr. Mater.* **2005**, *53*, 723–728. [CrossRef]
16. Zhang, Y.; Jiang, Z.B.; Sun, S.K.; Guo, W.-M.; Chen, Q.-S.; Qiu, J.-X.; Plucknett, K.; Lin, H.-T. Microstructure and mechanical properties of high-entropy borides derived from boro/carbothermal reduction. *J. Eur. Ceram. Soc.* **2019**, *39*, 3920–3924. [CrossRef]
17. Yan, X.L.; Constantin, L.; Lu, Y.F.; Silvain, J.-F.; Nastasi, M.; Cui, B. $(Hf_{0.2}Zr_{0.2}Ta_{0.2}Nb_{0.2}Ti_{0.2})C$ high-entropy ceramics with low thermal conductivity. *J. Am. Ceram. Soc.* **2018**, *101*, 4486–4491. [CrossRef]
18. Deng, S.; He, G.; Yang, Z.; Wang, J.; Li, J.; Jiang, L. Calcium-magnesium-alumina-silicate (CMAS) resistant high entropy ceramic $(Y_{0.2}Gd_{0.2}Er_{0.2}Yb_{0.2}Lu_{0.2})_2Zr_2O_7$ for thermal barrier coatings. *J. Mater. Sci. Technol.* **2022**, *107*, 259–265. [CrossRef]
19. Agyapong, J.; Mateos, D.; Czekanski, A.; Boakye-Yiadom, S. Investigation of effects of process parameters on microstructure and fracture toughness of SLM CoCrFeMnNi. *J. Alloys Compd.* **2024**, *987*, 173998. [CrossRef]
20. Chai, J.; Zhu, Y.; Shen, T.; Liu, Y.; NIU, L.; LI, S.; Jin, P.; Cui, M.; Wang, Z. Assessing fracture toughness in sintered Al_2O_3-ZrO_2(3Y)-SiC ceramic composites through indentation technique. *Ceram. Int.* **2020**, *46*, 27143–27149. [CrossRef]
21. Huang, H.L.; Jia, Z.H.; Xing, Y.; Wang, X.-L.; Liu, Q. Microstructure of Al-Si-Mg alloy with Zr/Hf additions during solidification and solution treatment. *Rare Mater.* **2019**, *38*, 1033–1042. [CrossRef]
22. Zhang, P.; Chen, C.; Chen, Z.; Shen, C.; Feng, P. Vacuum rapid fabrication of (Nb, Ti, Cr) Si_2 coatings with Mo, W addition: Microstructure and oxidation resistance at 1450 °C. *Vacuum* **2019**, *164*, 286–292. [CrossRef]
23. Chinese Society for Metals (CSM); The Minerals, Metals & Materials Society (TMS). Separation of zirconium and hafnium: A review. In *Energy Materials 2014*; Spinger: Berlin/Heidelberg, Germany, 2016.
24. Kim, S.J.; Yoon, K.N.; Ko, W.-S.; Park, E.S. Entropy-stabilized silicides: Expanding the B20 single-phase region from mono-silicide to high-entropy silicide. *APL Mater.* **2022**, *10*, 121105. [CrossRef]
25. Safarzadeh, M.; Chee, C.F.; Ramesh, S.; Fauzi, M.A. EEffect of sintering temperature on the morphology, crystallinity and mechanical properties of carbonated hydroxyapatite (CHA). *Ceram. Int.* **2020**, *46*, 26784–26789. [CrossRef]
26. Rice, R.W. Limitations of pore-stress concentrations on the mechanical properties of porous materials. *J. Mater. Sci.* **1997**, *32*, 4731–4736. [CrossRef]

27. Ji, M.; Xu, J.; Yu, D.; Chen, M.; El Mansori, M. Influence of sintering temperatures on material properties and corresponding milling machinability of zirconia ceramics. *J. Manuf. Process.* **2021**, *68*, 646–656. [CrossRef]
28. Nie, X.W.; Lu, Q. Fracture toughness of ZrO_2-SiC/$MoSi_2$ composite ceramics prepared by powder metallurgy. *Ceram. Int.* **2021**, *47*, 19700–19708. [CrossRef]
29. Lai, S.; Zang, J.; Shen, W.; Huang, G.; Fang, C.; Zhang, Y.; Chen, L.; Wang, Q.; Wan, B.; Jia, X.; et al. High hardness and high fracture toughness B_4C-diamond ceramics obtained by high-pressure sintering. *J. Eur. Ceram. Soc.* **2023**, *43*, 3090–3095. [CrossRef]
30. Cheng, L.; Xie, Z.; Liu, G.; Liu, W.; Xue, W. Densification and mechanical properties of TiC by SPS-effects of holding time, sintering temperature and pressure condition. *J. Eur. Ceram. Soc.* **2012**, *32*, 3399–3406. [CrossRef]
31. Saufi, A.S.M.; Singh, R.; Lee, K.Y.S.; Wu, T. Densification and mechanical properties of alumina ceramics via two-step sintering with different holding times. *Int. J. Eng. Mater. Manuf.* **2021**, *6*, 299–304.
32. Zhao, S.; Dai, Y.; Qin, F.; Li, Y.; Liu, L.; Zan, Z.; An, T.; Chen, P.; Gong, Y.; Wang, Y. On mode II fracture toughness of sintered silver based on end-notch flexure (ENF) test considering various sintering parameters. *Mater. Sci. Eng. A* **2021**, *823*, 141729. [CrossRef]
33. Sharif, A.A.; Misra, A.; Petrovic, J.J.; Mitchell, T. Alloying of $MoSi_2$ for improved mechanical properties. *Intermetallics* **2001**, *9*, 869–873. [CrossRef]
34. Liu, L.; Zhang, L.; Liu, D. Complete elimination of pest oxidation by high entropy refractory metallic silicide $(Mo_{0.2}W_{0.2}Cr_{0.2}Ta_{0.2}Nb_{0.2})Si_2$. *Scr. Mater.* **2020**, *189*, 25–29. [CrossRef]
35. Kuang, J.; Zhang, P.; Wang, Q.; Hu, Z.; Liang, X.; Shen, B. Formation and oxidation behavior of refractory high-entropy silicide (NbMoTaW)Si_2 coating. *Corros. Sci.* **2022**, *198*, 110134. [CrossRef]
36. Xiao, Z.; Zhang, L.; Guo, Z. Ab initio investigation of phase stability, thermo-physical and mechanical properties of $(Mo_{0.2}Cr_{0.2}Ta_{0.2}Nb_{0.2}X_{0.2})Si_2$ (X = W, V) high-entropy refractory metal silicides. *Comput Mater Sci.* **2022**, *203*, 111116. [CrossRef]
37. Gild, J.; Braun, J.; Kaufmann, K.; Marin, E.; Harrington, T.; Hopkins, P.; Vecchio, K.; Luo, J. A high-entropy silicide: $(Mo_{0.2}Nb_{0.2}Ta_{0.2}Ti_{0.2}W_{0.2})Si_2$. *J. Mater.* **2019**, *5*, 337–343. [CrossRef]

Disclaimer/Publisher's Note: The statements, opinions and data contained in all publications are solely those of the individual author(s) and contributor(s) and not of MDPI and/or the editor(s). MDPI and/or the editor(s) disclaim responsibility for any injury to people or property resulting from any ideas, methods, instructions or products referred to in the content.